Journal of Computational and Applied Mathematics 236 (2012) 4882–4892

Contents lists available at SciVerse ScienceDirect

Journal of Computational and Applied Mathematics

journal homepage: www.elsevier.com/locate/cam

Multiscale simulations of concrete mechanical tests

Jan Vorel *, Vít Šmilauer, Zdeněk Bittnar

Department of Mechanics, Faculty of Civil Engineering, Czech Technical University in Prague, Thákurova 7, 166 29 Praha 6, Czech Republic

ARTICLE INFO

Article history:
Received 4 September 2011
Received in revised form 7 November 2011

Keywords:
Mori–Tanaka method
Concrete
Mortar
Virtual testing
Multiscale modeling
Coated inclusion

ABSTRACT

In civil engineering, computational modeling is widely used in the design process at the structural level. In contrast to that, an automated support for the selection or design of construction materials is currently not available. Specification of material properties and model parameters has a strong influence on the results. Therefore, an uncoupled two-step approach is employed to provide relatively quick and reliable simulations of concrete (mortar) tests. First, the Mori–Tanaka method is utilized to include the majority of small aggregates and air voids. The strain incremental form of MT approach serves for the prediction of material properties subsequently used in the finite element simulations of mechanical tests.

1. Introduction

In civil engineering, computational modeling is widely used in the design process at the structural level. Powerful commercial packages based on the theory of beams, plates and shells and on the finite element method (FEM) have been developed for a structural analysis and are nowadays considered as one of the fundamental design tools. In contrast to that, an automated support for the selection or design of construction materials is currently not available. Specification of material properties and model parameters needed for the structural analysis is a crucial task and has a strong influence on the results. This is especially important if the influence of mix composition, processing steps and environmental conditions during the construction stage on the long-term durability of the structure needs to be evaluated. Values of concrete parameters could be determined by experiments, but this is a time-consuming, tedious process that can considerably slow down the design process. Therefore, a virtual testing tool, i.e. integrated set of models, algorithms and procedures for the prediction of mechanical properties of materials, seems to be an attractive alternative.

Nowadays, the most used construction material is concrete, which is a complex composite material over a wide range of length scales from nanometer to meter. The main objective of our work is to develop a virtual testing tool for concrete which will provide the material parameters for existing numerical models based on basic material data of individual components. At present, attention is limited to the mechanical part of concrete response.

Concrete belongs to a large group of particle reinforced composites where the particle phase can be considered as random, applying not only to particle position but also to its size and orientation, which projects into the material isotropy on the macro-scale. Reasonable approximation can then be constructed with limited information such as grading curve (particle size distribution function), particle shape factor and their volume fraction with no need for microstructure images. Note that considering a large range of particle sizes results in a complex finite element model with too many elements. Such structures are then computationally very expensive particularly in the view of complicated numerical simulations of damage processes in concrete. Therefore, an uncoupled two-step approach is employed in this paper to provide relatively quick and reliable simulations of concrete tests, e.g. three-point bending tests. First, the Mori–Tanaka (MT) method [1] is utilized to include the

* Corresponding author. Tel.: +420 224354495; fax: +420 224310775.
E-mail addresses: jan.vorel@fsv.cvut.cz (J. Vorel), smilauer@cml.fsv.cvut.cz (V. Šmilauer), bittnar@fsv.cvut.cz (Z. Bittnar).

0377-0427/$ – see front matter © 2012 Elsevier B.V. All rights reserved.
doi:10.1016/j.cam.2012.01.009

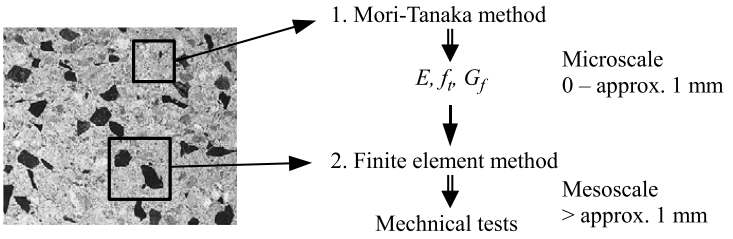

Fig. 1. Computational scheme.

Table 1
Mix composition of three different types used for experiments (SP stands for superplasticizer Glenium ACE 40).

Label	Cement (g)	Silica sand (mm)			SP/cement (mass) (%)	w/c (−)
		0–0.25	0.25–1	1–2		
P0	1400	0	0	0	0.2	0.35
P1	450	0	0	1350	0.5	0.35
P2	450	450	450	450	0.5	0.35

Table 2
Material properties (·* Calculated values from experiments).

Material	E (GPa)	ν (−)	f_t (MPa)	G_f (N/m)
Cement paste ($\cdot_3$)	10.0*	0.2	5.8*	15.9*
Silica sand ($\cdot_1$)	70.0	0.17	50.0	55
Air voids ($\cdot_4$)	10^{-4}	0	–	–

majority of small aggregates and air voids. The strain incremental form of MT approach serves for the prediction of material properties (tensile strength f_t, Young's modulus E, Poisson's ratio ν, fracture energy G_f) subsequently used in the finite element simulations of mechanical tests. Only large particles are involved as these are decisive for the onset and evolution of damage; see Fig. 1 for illustration.

The scale bridging is provided by the material parameters derived on the microscale (f_t, E, ν, G_f), i.e. homogenized material properties (material law) are embedded into an integration point of an upscale finite element. The choice of the localization limiter for the microscale is based on the crack band theory and is set to 2.5 times the maximum aggregate size of a given mix; see Section 3.

The paper is organized as follows. Section 2 describes indispensable experiments and results utilized for the setup and verification of the proposed methodology. Next section introduces the modified Mori–Tanaka scheme for the determination of homogenized material properties of concrete. In Section 4, a finite element method based approach is described.

2. Experiments

As already stated in the introductory part, the paper focuses on a computational side. However, no numerical predictions can be validated if not supported by proper experimental data [2]. Therefore, the objective of the experimental program in the context of the present study is to verify the proposed numerical approach. It is noteworthy that present mixtures represent rather mortar than concrete as seen in Table 1. Nevertheless, the proposed approach is still applicable to other material systems including concrete or asphalt mixtures; see e.g. [3].

Table 1 gives the composition of mixtures used in the present experiments. Three mixtures with different grading curves of silica sand are utilized. A mix containing ordinary Portland cement 42.5 R is employed as a binder with the water/cement ratio $(w/c) = 0.35$. To ensure a proper workability of mixtures the superplasticizer (SP) Glenium ACE 40 is added.

From each mix three prisms ($40 \times 40 \times 160$ mm) were cast horizontally and vibrated for 2 min. The molds were stored for 24 h in the climate box and then stored in water saturated with calcium hydroxide. After 28 days each specimen was cut into parts (approx. $20 \times 20 \times 80$ mm) which were adopted for the three-point bending test and subsequently for the compression test. The results are summarized in Table 2. Note that inverse analysis of three-point bending test is performed to determine the Young modulus and tensile strength for the cement paste (i.e. P0 specimen).

3. Microscale

A numerical prediction of the non-linear behavior of concrete on a microscale is described in this section. The obtained material properties are then utilized for the finite element simulations at the mesoscopic level. The mean field approach is utilized to grasp the real microstructure and grading curve. Therefore, concrete is seen as a four-phase system (Fig. 2(b)):

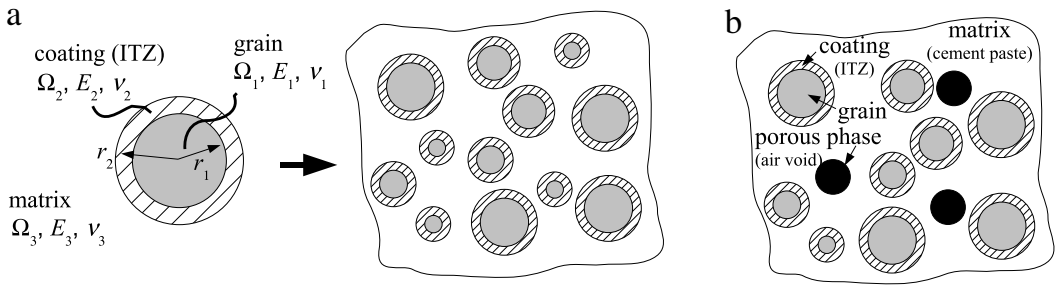

Fig. 2. (a) A two-layer spherical inclusion embedded in an infinite matrix, (b) representation of a representative volume element on the microscale.

- aggregates, phase 1 ($\cdot_1$);
- coating (interfacial transition zone (ITZ) around aggregates), phase 2 ($\cdot_2$);
- matrix (hydrated cement and water), phase 3 ($\cdot_3$);
- porous phase (air voids), phase 4 ($\cdot_4$).

In the present study, material properties of a hardened cement paste (matrix) are assumed to be known from experimental tests presented in the previous section. If the properties of cement paste are not experimentally determined, they can be evaluated e.g. on the basis of micromechanical models; see [4,5] for more details.

The Mori–Tanaka approach is a well known method belonging to mean field procedures and providing quick and reliable estimates of effective properties when having only limited information about the microstructure. There, the effect of interaction of the inclusions is accounted for by assuming that the stress in each phase is equal to that of a single inclusion embedded into an unbounded matrix subjected to as yet unknown average strain ($\langle\vec{\varepsilon}_3\rangle$) or stress ($\langle\vec{\sigma}_3\rangle$) in a matrix phase; see e.g. [6,7] for further details.

The local strain field in the inhomogeneities can be then written in terms of the partial strain concentration factor $\mathbf{A}_r^{dil}$ or the strain concentration factor $\mathbf{A}_r^{\mathrm{MT}}$ provided by the MT method as

$$\left\langle\vec{\varepsilon}^{\,(r)}\right\rangle = \mathbf{A}_r^{dil}\left\langle\vec{\varepsilon}^{\,(m)}\right\rangle = \mathbf{A}_r^{\mathrm{MT}}\left\langle\vec{\varepsilon}\,\right\rangle. \tag{1}$$

Assuming only isotropic spherical inclusions (both coated and uncoated) in an isotropic matrix, the effective properties can be determined in terms of the effective bulk $\left(K^{\mathrm{MT}}\right)$ and shear $\left(\mu^{\mathrm{MT}}\right)$ moduli which are derived through the well known relations

$$K^{\mathrm{MT}} = K_m + \sum_{r=1}^{N} c_r\,(K_r - K_m)\,A_r^{\mathrm{MT},K}, \tag{2}$$

$$\mu^{\mathrm{MT}} = \mu_m + \sum_{r=1}^{N} c_r\,(\mu_r - \mu_m)\,A_r^{\mathrm{MT},\mu}, \tag{3}$$

where $\cdot_m$ refers to the matrix phase, N is the number of different phases and c_r is the corresponding volume fraction of the r-th phase. The strain concentration factor is then provided by

$$A_r^{\mathrm{MT},f} = \frac{A_r^{dil,f}}{c_m + \sum_{r=1}^{N} c_r A_r^{dil,f}}, \quad \text{with } f = K, \mu. \tag{4}$$

Partial concentration factors $A_r^{dil,f}$ are defined in Eqs. (13), (27) and (30). The concentration factor for the matrix phase can be determined from

$$c_m A_m^{\mathrm{MT},f} + \sum_{r=1}^{N} c_r A_r^{\mathrm{MT},f} = 1. \tag{5}$$

3.1. Spherical coordinate system

The basic relations and transformations utilized for the derivation of concentration factors are briefly summarized hereafter. The spherical coordinate system (r, θ, ϕ) written in terms of corresponding Cartesian coordinates (x_1, x_2, x_3) reads

$$r = \sqrt{x_1^2 + x_2^2 + x_3^2}, \qquad \theta = \arccos\left(\frac{x_3}{r}\right), \qquad \phi = \arctan\left(\frac{x_2}{x_1}\right). \tag{6}$$

Conversely, the Cartesian coordinates are given by

$$x = r\sin\theta\cos\phi, \qquad y = r\sin\theta\sin\phi, \qquad z = r\cos\theta, \tag{7}$$

where $r \in \langle 0, \infty)$, $\theta \in \langle 0, \pi\rangle$, $\phi \in \langle 0, 2\pi)$. The transformation between the unit vectors in both coordinate systems follows from

$$\begin{Bmatrix} j_r \\ j_\theta \\ j_\phi \end{Bmatrix} = \begin{bmatrix} \sin\theta\cos\phi & \sin\theta\sin\phi & \cos\theta \\ \cos\theta\cos\phi & \cos\theta\sin\phi & -\sin\theta \\ -\sin\phi & \cos\phi & 0 \end{bmatrix} \begin{Bmatrix} j_1 \\ j_2 \\ j_3 \end{Bmatrix}, \tag{8}$$

where $\{j_r, j_\theta, j_\phi\}^{\mathsf{T}}$ stands for the unit vector in the spherical coordinate system and $\{j_1, j_2, j_3\}^{\mathsf{T}}$ is the unit vector in Cartesian coordinates. The volume averaging of a quantity $f(r, \theta, \phi)$ for a spherical shell takes the form

$$\langle f\rangle = \frac{1}{4/3\pi\left(r_{\text{out}}^3 - r_{\text{in}}^3\right)} \int_0^{2\pi}\int_0^{\pi}\int_{r_{\text{in}}}^{r_{\text{out}}} f(r, \theta, \phi)\ \mathrm{d}r\,\mathrm{d}\theta\,\mathrm{d}\phi, \tag{9}$$

where r_{out} and r_{in} are the outer and inner radii.

The elastic constitutive equation (elasticity law) reads

$$\vec{\sigma} = \mathbf{L}\vec{\varepsilon}, \tag{10}$$

where $\mathbf{L}$ refers to the stiffness matrix and for an isotropic material written in terms of bulk (K) and shear moduli (μ) receives the form

$$\mathbf{L} = \begin{bmatrix} K+4\mu/3 & K-2\mu/3 & K-2\mu/3 & 0 & 0 & 0 \\ & K+4\mu/3 & K-2\mu/3 & 0 & 0 & 0 \\ & & K+4\mu/3 & 0 & 0 & 0 \\ & \text{symmetric} & & \mu & 0 & 0 \\ & & & & \mu & 0 \\ & & & & & \mu \end{bmatrix}. \tag{11}$$

The components of the strain vector in spherical coordinates utilized for derivation of concentration factors are given by

$$\begin{Bmatrix} \varepsilon_{rr} \\ \varepsilon_{\theta\theta} \\ \varepsilon_{\phi\phi} \\ \varepsilon_{\theta\phi} \\ \varepsilon_{\phi r} \\ \varepsilon_{r\theta} \end{Bmatrix} = \begin{Bmatrix} \dfrac{\partial u_r}{\partial r} \\ \dfrac{1}{r}\left(\dfrac{\partial u_\theta}{\partial\theta} + u_r\right) \\ \dfrac{1}{r\sin\theta}\left(\dfrac{\partial u_\phi}{\partial\phi} + u_r\sin\theta + u_\theta\cos\theta\right) \\ \dfrac{1}{2r}\left(\dfrac{1}{\sin\theta}\dfrac{\partial u_\theta}{\partial\phi} + \dfrac{\partial u_\phi}{\partial\theta} - u_\phi\cot\theta\right) \\ \dfrac{1}{2}\left(\dfrac{1}{r\sin\theta}\dfrac{\partial u_r}{\partial\phi} + \dfrac{\partial u_\phi}{\partial r} - \dfrac{u_\phi}{r}\right) \\ \dfrac{1}{2}\left(\dfrac{1}{r}\dfrac{\partial u_r}{\partial\theta} + \dfrac{\partial u_\theta}{\partial r} - \dfrac{u_\theta}{r}\right) \end{Bmatrix}. \tag{12}$$

3.2. Uncoated inclusion

The partial concentration factors $\left(A_r^{dil,f}\right)$ for a spherical inclusion in an isotropic matrix (i.e. air voids) can be determined on the basis of the Eshelby solution as

$$A_r^{dil,K} = \frac{K_m}{K_m + S^K(K_r - K_m)}, \qquad A_r^{dil,\mu} = \frac{\mu_m}{\mu_m + S^\mu(\mu_r - \mu_m)}, \tag{13}$$

where [8,9]

$$S^K = \frac{3K_m}{3K_m + 4\mu_m}, \qquad S^\mu = \frac{6}{5}\frac{K_m + 2\mu_m}{3K_m + 4\mu_m}. \tag{14}$$

3.3. Coated inclusion

This section is concerned with the derivation of partial concentration factors of an isotropic two-layered spherical inclusion embedded in an isotropic matrix according to [10,11]. To simplify the notation let the central core phase, coating and matrix be denoted by indexes 1, 2 and 3, respectively, as seen in Fig. 2(a). To obtain the desired formulas we split the

state of deformation into the bulk and deviatoric parts while exploiting the spherical coordinate system with the origin located at the center of the concentric spheres.

3.3.1. Hydrostatic pressure

When the uniform strain condition

$$\varepsilon_{rr}^0 = \frac{\varepsilon_v^0}{3}, \tag{15}$$

is prescribed at infinity the boundary displacements are given in the form

$$\vec{u} = r\frac{\varepsilon_v^0}{3}\vec{j}_r, \tag{16}$$

where ε_v^0 is the constant and $\vec{j}_r = \{1, 0, 0\}^{\mathsf{T}}$ stands for the first vector of the spherical coordinate system. Due to the spherical symmetry of the problem, the task reduces to the one-dimensional solution. The displacements u_θ, u_ϕ vanish and the non-zero displacement for the (i)-th phase is [12]

$$u_r{}^{(i)} = B_1{}^{(i)} r + \frac{B_2{}^{(i)}}{r^2}, \tag{17}$$

where $B_1{}^{(i)}$ and $B_2{}^{(i)}$ are constants. Now, consider an inclusion displayed in Fig. 2(a) where the continuity conditions of stresses $\sigma_{rr}{}^{(i)}$ and displacements $u_r{}^{(i)}$ have to be fulfilled at all interfaces between the phases.

Note, that the coefficient $B_2{}^{(1)}$ is equal to zero to avoid singularity at the origin and $B_1{}^{(3)}$ is determined by the applied strain at infinity. The solution of the resulting set of equations can be found in [10].

3.3.2. Simple shear

Assume that the body is loaded by the shear strain γ in the Cartesian coordinate system. The displacements then take the form

$$u_{x_1} = \gamma x_1, \qquad u_{x_2} = -\gamma x_2, \qquad u_{x_3} = 0. \tag{18}$$

Using Eqs. (7) and (8) renders the displacements in the spherical coordinate system as

$$\begin{aligned} u_r &= \gamma r \sin^2\theta \cos 2\phi = U_r(r) \sin^2\theta \cos 2\phi, \\ u_\theta &= \gamma r \sin\theta \cos\theta \cos 2\phi = U_\theta(r) \sin\theta \cos\theta \cos 2\phi, \\ u_\phi &= -\gamma r \sin\theta \sin 2\phi = U_\phi(r) \sin\theta \sin 2\phi, \end{aligned} \tag{19}$$

with $U_\phi = -U_\theta$. Substituting Eq. (19) into the equilibrium conditions yields the general solution

$$\begin{aligned} U_r{}^{(i)} &= C_1{}^{(i)} r - \frac{6\nu_i}{1-2\nu_i} C_2{}^{(i)} r^3 + \frac{3C_3{}^{(i)}}{r^4} + \frac{5-4\nu_i}{1-2\nu_i}\frac{C_4{}^{(i)}}{r^2}, \\ U_\theta{}^{(i)} &= C_1{}^{(i)} r - \frac{7-4\nu_i}{1-2\nu_i} C_2{}^{(i)} r^3 - \frac{2C_3{}^{(i)}}{r^4} + \frac{2C_4{}^{(i)}}{r^2}, \end{aligned} \tag{20}$$

where $C^{(i)}$'s are constants. Similar to the hydrostatic pressure $C_3{}^{(1)}$ and $C_4{}^{(1)}$ are set equal to zero to avoid singularity and $C_2{}^{(3)}$ is equal to zero to ensure the boundary conditions at infinity. The solution given in [10,11,13] is briefly reviewed here to allow for the derivation of partial concentration factors. The continuity condition of the displacements and stresses have to be accomplished at interfaces. Note, that only four conditions are independent and read

$$\mathbf{D}_i(r_i)\,\vec{W}^{(i)} = \mathbf{D}_{i+1}(r_i)\,\vec{W}^{(i+1)}, \tag{21}$$

where $\vec{W}^{(i)} = \left\{C_1{}^{(i)}, C_2{}^{(i)}, C_3{}^{(i)}, C_4{}^{(i)}\right\}^{\mathsf{T}}$ and

$$\mathbf{D}_i(r) = \begin{bmatrix} r & -\dfrac{6\nu_i}{1-2\nu_i} r^3 & \dfrac{3}{r^4} & \dfrac{5-4\nu_i}{(1-2\nu_i)\,r^2} \\ r & -\dfrac{7-4\nu_i}{1-2\nu_i} r^3 & -\dfrac{2}{r^4} & \dfrac{2}{r^2} \\ \mu_i & \dfrac{3\nu_i}{1-2\nu_i}\mu_i r^2 & -\dfrac{12\mu_i}{r^5} & \dfrac{2(\mu_i-5)\,\mu_i}{(1-2\nu_i)\,r^3} \\ \mu_i & -\dfrac{7+2\mu_i}{1-2\nu_i}\mu_i r^2 & \dfrac{8\mu_i}{r^5} & \dfrac{2(1+\mu_i)\,\mu_i}{(1-2\nu_i)\,r^3} \end{bmatrix}. \tag{22}$$

The solution of the system of Eqs. (21) is written as

$$\vec{W}^{(i+1)} = \mathbf{D}_{i+1}{}^{-1}(r_i)\,\mathbf{D}_i(r_i)\,\vec{W}^{(i)} = \mathbf{M}^{(i)}\vec{W}^{(i)} = \prod_{k=1}^{i}\mathbf{M}^{(k)}\vec{W}^{(1)} = \mathbf{P}^{(i)}\vec{W}^{(1)}. \tag{23}$$

After some algebra we obtain all coefficients in the form

$$C_1{}^{(1)} = P_{22}{}^{(2)} \frac{C_1{}^{(3)}}{P_{11}{}^{(2)}P_{22}{}^{(2)} - P_{12}{}^{(2)}P_{21}{}^{(2)}},$$
$$C_2{}^{(1)} = -P_{21}{}^{(2)} \frac{C_1{}^{(3)}}{P_{11}{}^{(2)}P_{22}{}^{(2)} - P_{12}{}^{(2)}P_{21}{}^{(2)}},$$
$$\vec{W}^{(i)} = \frac{C_1{}^{(3)}}{P_{11}{}^{(2)}P_{22}{}^{(2)} - P_{12}{}^{(2)}P_{21}{}^{(2)}} \mathbf{P}^{(i-1)} \begin{bmatrix} P_{22}{}^{(2)} \\ -P_{21}{}^{(2)} \\ 0 \\ 0 \end{bmatrix}, \quad i = 2, 3, \tag{24}$$

where $C_1{}^{(3)} = \gamma$.

3.3.3. Concentration factors

The average strain in each phase can be calculated using Eq. (9). When a uniform strain condition

$$\vec{\varepsilon}^0 = \frac{\varepsilon_v^0}{3}\mathbf{I} + \vec{e}^0, \tag{25}$$

is prescribed at infinity the volumetric average strain takes the form

$$\left\langle \varepsilon_v^{(i)} \right\rangle = \frac{B_1{}^{(i)}}{B_1{}^{(3)}} \varepsilon_v^0 = A_i^{dil,K} \varepsilon_v^0. \tag{26}$$

Adopting the known solution for constants $B^{(i)}$'s (see [10]), we arrive at

$$A_1^{dil,K} = (3K_2 + 4\mu_2)(3K_3 + 4\mu_3)/p,$$
$$A_2^{dil,K} = (3K_1 + 4\mu_2)(3K_3 + 4\mu_3)/p, \tag{27}$$

where

$$p = (3K_1 + 4\mu_2)(3K_2 + 4\mu_3) + 12c(K_2 - K_1)(\mu_3 - \mu_2), \tag{28}$$

with $c = (r_1/r_2)^3$.

The average deviatoric strain reads [10]

$$\left\langle \vec{e}^{(i)} \right\rangle = \frac{1}{C_1{}^{(3)}} \left[C_1{}^{(i)} - \frac{21}{5} \frac{r_i^5 - r_{i-1}^5}{(1-2\nu_2)\left(r_i^3 - r_{i-1}^3\right)} C_2{}^{(i)} \right] \vec{e}^0 = A_i^{dil,\mu} \vec{e}^0. \tag{29}$$

The partial deviatoric concentration factors for individual phases then become

$$A_1^{dil,\mu} = \frac{1}{C_1{}^{(3)}} \left(C_1{}^{(1)} - \frac{21}{5} \frac{r_1^2}{1-2\nu_1} C_2{}^{(1)} \right),$$
$$A_2^{dil,\mu} = \frac{1}{C_1{}^{(3)}} \left(C_1{}^{(2)} - \frac{21}{5} \frac{r_2^5 - r_1^5}{(1-2\nu_2)\left(r_2^3 - r_1^3\right)} C_2{}^{(2)} \right). \tag{30}$$

3.4. Mori–Tanaka scheme

An incremental form of the MT method is adopted to address a quasi-brittle behavior of concrete and to obtain the whole loading path in a uniaxial tension. The matrix and coating phase are seen as isotropic material with the isotropic damage, i.e. stiffness moduli corresponding to different directions decrease proportionally and independently of the loading direction. The aggregates and air voids are assumed to be purely isotropic. A sample is incrementally loaded by the strain and the corresponding stress is calculated with respect to the evolved damage; see Fig. 3. It is noteworthy to mention that the strain-softening results from an evolution of micro-cracks and can be described by a micromechanics-based damage; see e.g. [14]. This approach could be a further extension of the proposed procedure and would involve a propagation of intersecting microcracks instead of constitutive equations.

Due to the lack of information about the coating phase and to keep the approach simple, we decided that the coating and matrix have the same damage parameter driven by the evolution of strain in the matrix; see Eqs. (1) and (5). An exponential softening stress–strain law is utilized and reads

$$\omega = 1 - \frac{\varepsilon_0}{\varepsilon_{eq}} \exp\left(-\frac{\varepsilon_{eq} - \varepsilon_0}{\varepsilon_f - \varepsilon_0} \right), \tag{31}$$

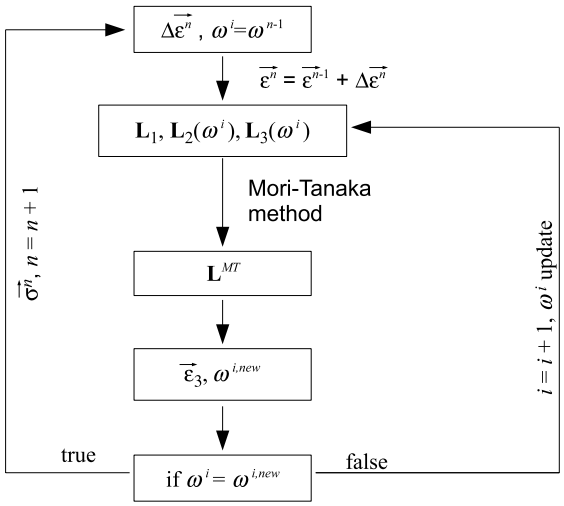

Fig. 3. The numerical scheme of the incremental form of the Mori–Tanaka method.

Table 3
Material properties of the interfacial transition zone (phase 2).

E_2 (GPa)	ν_2 (−)	Thickness (μm)
3.0	0.2	20

where $\varepsilon_f = G_f/f_t h$ stands for the fracturing strain, $\varepsilon_0 = f_t/E$ denotes the strain at the peak load and h is the crack band width. The equivalent strain ε_{eq} is a scalar measure derived from the strain tensor. Here, we adopt the Mazars definition based on a norm of positive part of strain

$$\varepsilon_{\text{eq}} = \sqrt{\sum_{I=1}^{3} \|\varepsilon_I\|^2}, \tag{32}$$

where $\|\varepsilon_I\|$ are positive parts of principal values of the strain tensor.

3.5. Numerical results and discussion

To verify the proposed numerical approach for an estimation of concrete properties, the computations are carried out for the mortars presented in Section 2. As mentioned above, the Mori–Tanaka method is employed to account for the fraction of small aggregates (2/3 of the total volume) not considered on the mesoscale (P1^p, P2^p). Moreover, in some simulations the whole grading curve is considered (P1, P2) and the obtained results are compared with the experimental data. Air voids present in the hardened specimens are taken into account as well. Therefore, the volume fractions of remaining components are adequately scaled; see Table 4.

As suggested, the resulting tensile stress–strain diagrams then serve for the evaluation of material properties, i.e. Young's modulus, tensile strength and fracture energy. To determine the value of the fracture energy the crack band theory is utilized. The width (h) of the strain-softening zone is assumed to be equal to $2.5d_0$, where d_0 stands for the maximum aggregate (heterogeneity) size [15] and is constant herein for all samples of mortar ($d_0 = 2$ mm) as evident from Table 4. For the cement paste, the band width is assumed as $2.5d_0 = 2.5 \times 0.4 = 1.0$ mm. The thickness of interfacial transition zone around the aggregates is adopted as proposed in [16]. Based on the analytical and experimental results, Yang [16] suggested that the average elastic modulus of a transition zone is about 20%–40% (30% is employed in present study) of the matrix modulus for the transition zone with a thickness of 20 μm. The corresponding volume fraction of coating is calculated with respect to generated aggregate sizes (volume of spherical shells). The material properties of individual phases are summarized in Tables 2 and 3. The aggregate sizes are generated according to the grading curve for each specimen. Four different sizes are randomly chosen considering a uniform distribution for each region of the curve. Fig. 4 shows the numerical results for 100 simulations for each material sample. The resulting average material parameters are summarized in Table 5. It is noteworthy that a stronger influence of smaller aggregates is pronounced for samples P2 and P2^p.

4. Mesoscale

The second step of the present procedure based on the finite element method is described in this section. Here, the large aggregates are introduced into the new homogenized matrix derived from the previous step to perform assumed virtual tests.

Table 4
Volume fractions of individual components ($\cdot^p$ composition used for a consequent simulations on a mesoscale).

Label	Cement paste & ITZ ($\cdot_{2,3}$)	Silica sand (mm) ($\cdot_1$)			Air voids ($\cdot_4$)
		0–0.25	0.25–1	1–2	
P1	0.34	0	0	0.51	0.15
P2	0.38	0.19	0.19	0.19	0.05
$P1^p$	0.41	0	0	0.41	0.18
$P2^p$	0.47	0.235	0.235	0	0.06

Table 5
Average material parameters obtained by Mori–Tanaka simulations and experiments.

Label	MT method				Exp. G_f (N/m)
	E (GPa)	ν (−)	f_t (MPa)	G_f (N/m)	
P1	13.9	0.19	6.7	55.6	53.6
P2	11.4	0.19	6.7	73.7	70.0
$P1^p$	11.6	0.19	6.2	59.0	–
$P2^p$	9.3	0.19	6.1	73.4	–

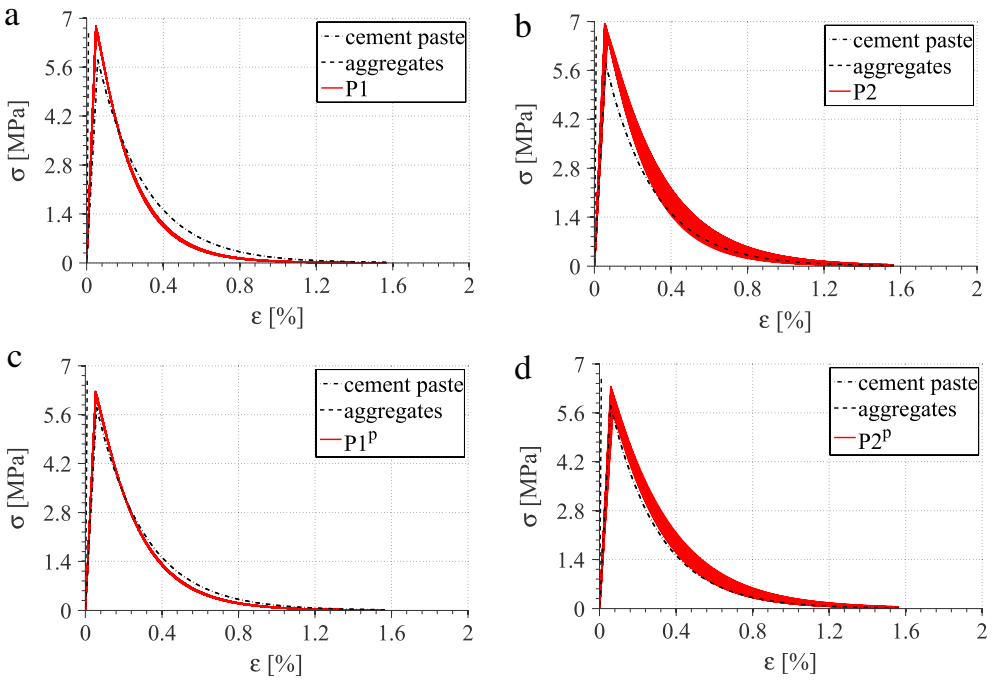

Fig. 4. Stress–strain diagrams for the Mori–Tanaka simulations: (a) P1 sample, (b) P2 sample, (c) $P1^p$, (d) $P2^p$.

It has been demonstrated that creating a numerical model presents a crucial step influencing reliability and accuracy of numerical predictions; see e.g. [17,18]. Here, the large aggregates (i.e. aggregates which are not involved in the MT scheme in previous step) are introduced into a new matrix phase with the material properties determined on the microscale (Table 5). Preparation of a concrete sample at a mesoscopic level suitable for two- and three-dimensional numerical simulations is described with the emphases on two essential steps: (i) geometry preparation and (ii) generation of finite element mesh. Note that isotropic damage material models with an exponential softening are employed for individual phases. Moreover, the equivalent strain (the Mazars definition) is assumed to take the same form as for the MT scheme; see Eq. (32).

4.1. Geometry generation

Generation of a numerical model in a realistic way follows a "take and place" method [19] to place aggregates with a specific orientation one by one at the right position. The generation mechanism is designed here to fulfill the following requirements.

- The size distribution function of aggregates (grading curve) in real concrete should be matched.
- Shapes of aggregates should be approximated in a realistic way. Note that only convex shapes of aggregates and the shape factor (Eq. (33)) are assumed.

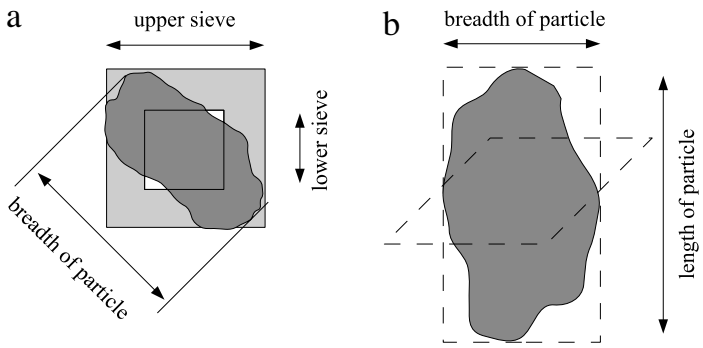

Fig. 5. Definition of aggregate: (a) breadth, (b) length.

- The minimum distance and volume control should be implemented.
- The periodicity of the aggregates crossing the model boundaries should be taken into account.

A generation procedure basically follows the steps mentioned above. First, a set of aggregates is created in accordance with a grading curve. The shape and size of aggregates is defined in this step. The aggregate shape can be seen as a sphere, ellipsoid or polytope (polyhedron for three-dimensional) and the breadth of the particle has to pass through a given upper sieve size and cannot be smaller than the lower sieve size; see Fig. 5 and [20] for more details. The length of the particle is given by the shape factor

$$\alpha = \frac{\text{length of particle}}{\text{breadth of particle}}. \tag{33}$$

Dimensions of all shapes are generated purely randomly with the only constrain to fit the prescribed interval of the specific part of the grading curve. Moreover, for the polytope shapes the number of vertices is also randomly generated in the appropriate limits. Whereas our interest is to obtain a reasonably good agreement of the response of virtual testing sample with true laboratory measurements, we still have to bear in mind the computational cost of such a simulation. Therefore, it is inevitable to implement into the generation procedures some control mechanisms which reduce the unsuitable small facets and angles in the particle.

When all aggregates are generated, they are taken out one by one from the aggregate database and randomly assigned positions and orientations and placed in the packing region. The larger aggregates are placed first to reduce overlapping and computational time. However, even if doing so the packed aggregates inevitably overlap each other, so that overlapping judgment is necessary for a successful numerical modeling. If some minimal distance between aggregates is required each particle is first slightly enlarged before placing and after a successful positioning it is brought back to its original shape.

The last control mechanism is employed only when the aggregate exceeds the model boundaries and the periodicity condition has to be fulfilled. In such a case the aggregate is divided into the required number of parts placed at relevant positions. In addition, to provide conforming meshes a checking procedure is invoked to ensure that the fractions of a given particle are not under some specified limits. The whole procedure described herein was implemented into the *MATLAB* high-level language and interactive environment [21]. The multi-parametric toolbox for MATLAB [22] is used to perform all operations with volumes including copying, merging, splitting, intersecting, etc.

4.2. Mesh generation

This technique implies the use of conforming finite element meshes. This might seem daunting since it requires not only incorporation of an arbitrary number of aggregates, but also a complicated structure of cement paste around. In the present study, these obstacles are overcome by employing the volumetric modeling capacities of the *ANSYS* package [23].

4.3. Numerical results and discussion

Several plane-stress simulations of three-point bending tests were carried out to address the influence of aggregates on the response at the mesoscopic level (Fig. 6). The simplification from three-dimensional to two-dimensional distributions of aggregates is admissible as seen from results below. Moreover, the complex three-dimensional structure is more computationally demanding compared to plane-stress simulations which in the present study involved approx. 2200 elements and the computational time (the laptop with Intel Core i7 CPU, 2.67 GHz) was approx. 30 s for one simulation. This predestinates the procedure for further utilization in an optimization process of concrete mixtures.

For each mixture (P1 and P2) specimen dimensions were chosen according to experiments (Table 6) and sets of five FE models for P1 and P2 mixtures (see Section 2) were prepared with a random distribution of remaining aggregates. The volume of randomly generated aggregates for all samples was considered equal to 1/3 of the total volume and the shape

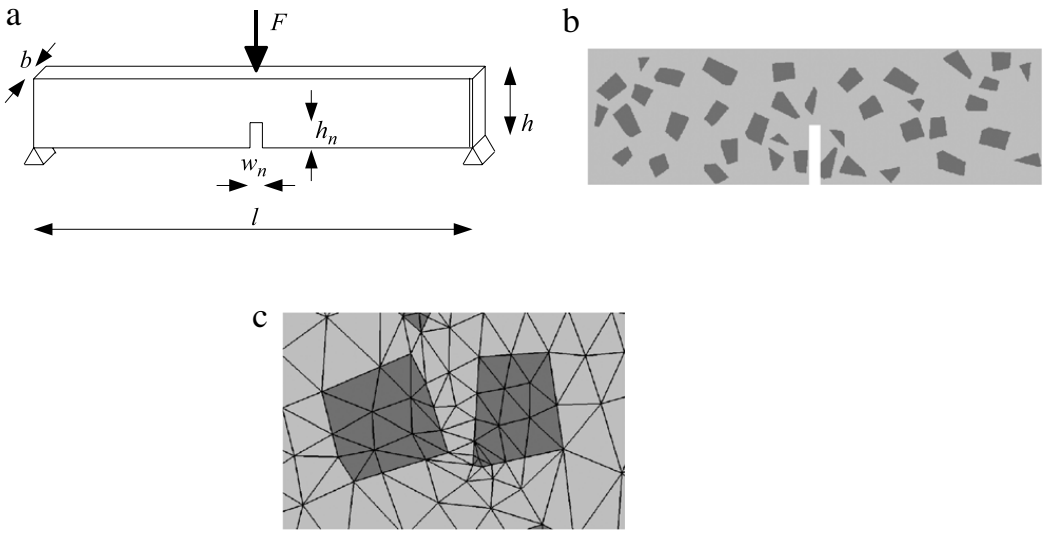

Fig. 6. Three-point bending test with notch: (a) scheme, (b) FE model, (c) zoom of FE mesh.

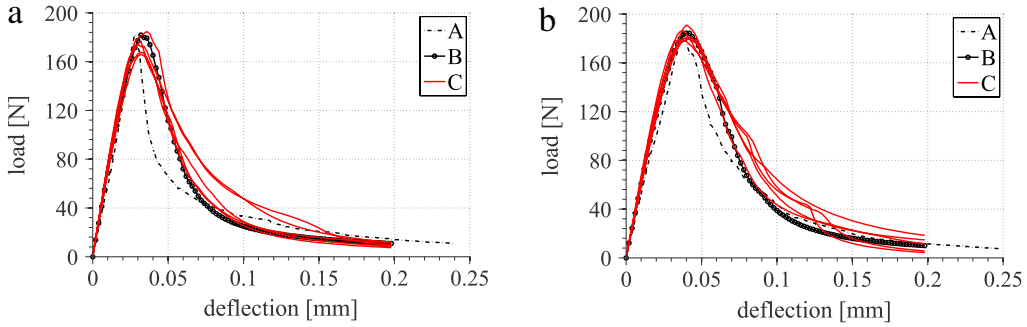

Fig. 7. Load–deflection diagrams for three-point bending tests (A—experiment, B—simulation for the material without aggregates assumed on the mesoscale, C—simulation with randomly distributed aggregates): (a) P1 samples, (b) P2 samples.

Table 6
Setup of three-point bending tests.

Label	l (mm)	h (mm)	b (mm)	w_n (mm)	h_n (mm)
P1	65.0	19.4	18.1	1.6	9.0
P2	65.0	19.2	18.3	1.6	8.5

factor was set between 1.0–1.5. The particle shapes were seen as polytopes to decrease the numerical cost of the present study [24]. Numerical analyses were performed in the OOFEM finite element code with the object oriented architecture for solving mechanical, transport and fluid mechanics problems [25].

An isotropic damage material model with exponential softening was assumed for all phases, i.e. the aggregates and homogenized cement paste. The material properties of aggregates are taken from Table 2 (silica sand) while the properties of surrounding matrices are summarized in Table 5 ($P1^p$, $P2^p$). Interfacial transition zone was not considered on the mesoscale. Triangular three-node constant strain plane-stress finite elements with 2 degrees of freedom in each node were utilized for a discretization.

The obtained average load–deflection diagrams are compared in Fig. 7. Generally, the peak load was reached for all presented simulations. Nevertheless, the post-peak response of finite element simulations exhibits a slightly higher fracture toughness. This is especially pronounced for the P1 samples where the separation of scales was not properly achieved due to the composition of grading curve; see Table 1. The simulations for P1 and P2 materials in Table 5, i.e. no aggregates were assumed on the mesoscale, are presented as well to advocate the Mori–Tanaka procedure utilized on the microscale.

5. Conclusions

A simple three-point bending test was examined in this paper to address two specific issues in the material modeling of concrete when limiting our information to a grading curve and material properties of individual constituents. On the one hand, the mesoscale simulations promoted the use of only major stone aggregates in the construction of a

simplified geometrical model thus considerably enhancing the computational efficiency while still reflecting, at least to some extent, the actual heterogeneity of concrete. On the other hand, they fully supported the proposed fully uncoupled two-scale modeling strategy with the material data of a mesoscale constitutive model of the binder phase derived from an independent lower scale homogenization step to account for the volume fraction of small aggregates excluded from mesoscale simulations. In the present case a set of virtual experiments was performed to provide the homogenized elastic properties, strength and fracture energy of the binder exploiting the Mori–Tanaka method as one of the most simple micromechanics models. A computational efficiency of this method combined with a simplified meso-scale computational model can thus be effectively used in the search for an optimized grading curve to meet specific requirements for a concrete composition. Moreover, the utilization of solely the Mori–Tanaka method could be suggested for determination of material properties as seen from the results in Fig. 7, but we should bear in mind that in the present study only limited grading curves were utilized and these results should not be overestimated and further investigation is demanded.

Acknowledgments

The financial support provided by the Czech Science Foundation grant No. 105/10/2400 and partially also by the research project CEZ MSM 6840770003 is gratefully acknowledged.

References

[1] J. Vorel, M. Šejnoha, Evaluation of homogenized thermal conductivities of imperfect carbon–carbon textile composites using the Mori–Tanaka method, Structural Engineering and Mechanics 33 (4) (2009) 429–446.
[2] W. Knauss, Perspectives in experimental solid mechanics, International Journal of Solids and Structures 37 (2000) 239–250.
[3] M. Šejnoha, R. Valenta, Selected chapters of mechanics of composite materials I, in: Micromechanical Modeling in Search for Macroscopic Constitutive Laws—Application to Asphalt, Technical University of Košice, 2011, pp. 189–248 (Chapter).
[4] B. Pichler, C. Hellmich, Upscaling quasi-brittle strength of cement paste and mortar: a multi-scale engineering mechanics model, Cement and Concrete Research 41 (5) (2011) 467–476.
[5] B. Pichler, C. Hellmich, J. Eberhardsteiner, Spherical and acicular representation of hydrates in a micromechanical model for cement paste: prediction of early-age elasticity and strength, Acta Mechanica 203 (3) (2009) 137–162.
[6] Y. Benveniste, A new approach to the application of Mori–Tanaka theory in composite materials, Mechanics of Materials 6 (1987) 147–157.
[7] Y. Benveniste, T. Chen, G. Dvorak, The effective thermal conductivity of composites reinforced by coated cyllindrically orthotropic fibers, Journal of Applied Physics 67 (6) (1990) 2878–2884.
[8] J. Eshelby, The determination of the elastic field of an ellipsoidal inclusion and related problems, Proceedings of the Royal Society of London Series A 241 (1957) 376–396.
[9] G. Weng, Some elastic properties of reinforced solids, with special reference to isotropic ones containing spherical inclusions, International Journal of Engineering Science 22 (7) (1984) 845–856.
[10] E. Herve, A. Zaoui, *n*-layered inclusion-based micromechanical modelling, International Journal of Engineering Science 31 (1) (1993) 1–10.
[11] H. Luo, G. Weng, On Eshelby's inclusion problem in a three-phase spherically concentric solid, and a modification of Mori–Tanaka's method, Mechanics of Materials 6 (4) (1987) 347–361.
[12] A. Love, A Treatise on the Mathematical Theory of Elasticity, Cambridge University Press, 1927.
[13] R. Christensen, Solutions for effective shear properties in three phase sphere and cylinder models, Journal of the Mechanics and Physics of Solids 27 (1979) 315–330.
[14] B. Pichler, C. Hellmich, H. Mang, A combined fracture-micromechanicsmodel for tensile strain-softening in brittle materials, based on propagation of interacting microcracks, International Journal for Numerical and Analytical Methods in Geomechanics 31 (2) (2007) 111–132.
[15] Z.P. Bažant, G. Pijaudier-Cabot, Measurement of characteristic length of nonlocal continuum, Journal of Engineering Mechanics 115 (4) (1989) 755–767.
[16] C. Yang, Effect of the transition zone on the elastic moduli of mortar, Cement and Concrete Research 28 (5) (1998) 727–736.
[17] J. Zeman, M. Šejnoha, From random microstructures to representative volume elements, Modelling and Simulation in Materials Science and Engineering 15 (2007) 325–335.
[18] J. Zeman, M. Šejnoha, Numerical evaluation of effective properties of graphite fiber tow impregnated by polymer matrix, Journal of the Mechanics and Physics of Solids 49 (1) (2001) 69–90.
[19] G. De Schutter, L. Taerwe, Random particle model for concrete based on delaunay triangulation, Materials and Structures 26 (2) (1993) 67–73.
[20] C. Mora, A. Kwan, H. Chan, Particle size distribution analysis of coarse aggregate using digital image processing, Cement and Concrete Research 28 (6) (1998) 921–932.
[21] MathWorks, Documentation for MATLAB, MathWorks, 2010. http://www.mathworks.com.
[22] M. Kvasnica, Real-Time Model Predictive Control via Multi-Parametric Programming: Theory and Tools, VDM Verlag, Saarbruecken, 2009.
[23] ANSYS, Inc., Documentation for ANSYS, ANSYS, Inc., 2005. Home page: http://www.ansys.com.
[24] J. Vorel, A. Kučerová, V. Šmilauer, Z. Bittnar, Virtual testing of concrete, in: Engineering Mechanics 2011, 2011, pp. 667–670.
[25] B. Patzák, Z. Bittnar, Design of object oriented finite element code, Advances in Engineering Software 32 (2001) 759–767. Home page: www.oofem.org.